A Coupled Model for Laplace's Tidal Equations in a Fluid with One Horizontal Dimension and Variable Depth

SAMUEL M. KELLY AND NICOLE L. JONES

The Oceans Institute, and School of Environmental Systems Engineering, University of Western Australia, Crawley, Western Australia, Australia

JONATHAN D. NASH

College of Earth, Ocean, and Atmospheric Sciences, Oregon State University, Corvallis, Oregon

(Manuscript received 9 August 2012, in final form 27 April 2013)

ABSTRACT

Tide–topography interactions dominate the transfer of tidal energy from large to small scales. At present, it is poorly understood how low-mode internal tides reflect and scatter along the continental margins. Here, the coupling equations for linear tides model (CELT) are derived to determine the independent modal solutions to Laplace's Tidal Equations (LTE) over stepwise topography in one horizontal dimension. CELT is (i) applicable to arbitrary one-dimensional topography and realistic stratification without requiring numerically expensive simulations and (ii) formulated to quantify scattering because it implicitly separates incident and reflected waves. Energy fluxes and horizontal velocities obtained using CELT are shown to converge to analytical solutions, indicating that "flat bottom" modes, which evolve according to LTE, are also relevant in describing tides over sloping topography. The theoretical framework presented can then be used to quantify simultaneous incident and reflected energy fluxes in numerical simulations and observations of tidal flows that vary in one horizontal dimension. Thus, CELT can be used to diagnose internal-tide scattering on continental slopes. Here, semidiurnal mode-1 scattering is simulated on the Australian northwest, Brazil, and Oregon continental slopes. Energy-flux divergence and directional energy fluxes computed using CELT are shown to agree with results from a finite-volume model that is significantly more numerically expensive. Last, CELT is used to examine the dynamics of two-way surface–internal-tide coupling. Semidiurnal mode-1 internal tides are found to transmit about 5% of their incident energy flux to the surface tide where they impact the continental slope. It is hypothesized that this feedback may decrease the coherence of sea surface displacement on continental shelves.

1. Introduction

The sun and moon generate tides in the ocean via the astronomical tide-generating force (ATGF; Newton 1687). Laplace (1776) derived the modern theory of linear inviscid tides for depth-uniform currents in an ocean of constant density [i.e., Laplace's Tidal Equations (LTE)]. In the early twentieth century, subsurface measurements of temperature revealed that the ocean is vertically stratified (e.g., Nansen 1902) and tidal-frequency motions vary with depth (Pettersson 1907). Miles (1974) formally rescaled the equations of motion to describe tides in a stratified ocean and allow for depth-varying currents. He found that depth-varying tidal motions separate into uncoupled vertical modes over a flat bottom (e.g., Rayleigh 1883), which individually obey LTE scaled by an equivalent depth. The zeroth mode, also known as the surface tide, has an equivalent depth that is very close to the actual ocean depth. It is effectively the depth-uniform motion originally described by Laplace. Higher modes ($n \geq 1$) have group speeds and vertical structures that are sensitive to density stratification. These modes are collectively known as the internal tide (e.g., Wunsch 1975) and have only been heavily researched for the last 50 years.

In many deep-ocean basins, where the ocean floor is mostly flat, it is useful to decompose tidal motions into vertical modes that evolve according to LTE because they have known horizontal wavelengths and group

Corresponding author address: Samuel Kelly, 7-321, Department of Mechanical Engineering, MIT, 77 Massachusetts Ave., Cambridge, MA 02139.
E-mail: samkelly@mit.edu

DOI: 10.1175/JPO-D-12-0147.1

speeds (e.g., Alford and Zhao 2007). However, in regions of sloping topography, vertical modes can be inconvenient because (i) they do not accommodate nonzero vertical velocity at sloping bottoms[1] and (ii) they become coupled where the water changes depth. Vertical-mode coupling over steep topography is evident in laboratory experiments (e.g., Zeilon 1912), analytical theories (e.g., Rattray 1960), numerical models (e.g., Baines 1982), and observations (e.g., Rudnick et al. 2003), which all display energy transfer between surface and internal tides.

Many investigations of tides in a stratified ocean avoid the complication of interpreting flat-bottom modes over sloping topography by simply examining the dynamics of the full, depth-dependent equations of motion. These models employ frameworks that do not require a flat bottom, such as ray tracing (e.g., Baines 1982), Green's functions (e.g., Echeverri and Peacock 2010), and finite-volume formulations (e.g., Carter et al. 2008). However, analyses of these models almost always return to concepts, such as surface–internal-tide decomposition, that are only well defined in terms of the modes that evolve according to LTE. A widespread reluctance to decompose tides over a sloping bottom into flat-bottom modes has produced diverse and nonstandardized definitions of surface and internal tides, which have led to ambiguous descriptions of tidal dynamics (see, e.g., Kelly et al. 2010; Gerkema 2011; Kelly and Nash 2011).

Fortunately, several studies have examined the behavior of flat-bottom modes over regions of sloping topography, which enables an unambiguous surface–internal-tide decomposition. Llewellyn Smith and Young (2002) coupled the modes that evolve according to LTE over small-scale topography with small gradients by linearizing the bottom-boundary condition. Later, Griffiths and Grimshaw (2007) coupled these modes over arbitrary topography. Most recently, Shimizu (2011) and Kelly et al. (2012) derived coupled energy balances for flat-bottom modes over arbitrary topography and Kelly et al. (2012) verified their accuracy in numerical simulations and observations.

While previous studies have demonstrated that tidal flows can be mathematically decomposed into flat-bottom modes over arbitrary topography, a conceptual model is desirable to interpret how these modes couple and evolve differently in domains with variable depth. Here, we present a semianalytical model that can accommodate arbitrary topography in one horizontal dimension but confines all variation in bottom depth to thin topographic steps. At all locations, the bottom is locally flat and motion evolves as uncoupled modal solutions to LTE (in Cartesian coordinates). The model is fundamentally similar to that of Griffiths and Grimshaw (2007), except that we have confined modal coupling to the matching conditions at each topographic discontinuity.

Several models have been developed that match the modal solutions to LTE at a single step (e.g., Rattray 1960; Rattray et al. 1969; Chapman and Hendershott 1981; St. Laurent et al. 2003; Klymak et al. 2011a). However, the model presented here accommodates an arbitrary number of steps and arbitrary depth-varying stratification. And, unlike the multistep model used by Sjöberg and Stigebrandt (1992), which was criticized by St. Laurent et al. (2003) because it did not couple the solutions between steps, the model presented here includes complete coupling between all steps (e.g., it exhibits resonance between double ridges; Echeverri et al. 2011; Klymak et al. 2013). Specifically, Sjöberg and Stigebrandt (1992) linearly superimposed the solutions from independent single-step solutions to estimate the cumulative energy flux radiating from complicated topographic shapes. In the model presented here, the matching conditions at each step are coupled to those at neighboring steps and the entire solution is obtained simultaneously (i.e., all steps within the domain are effectively coupled to one another). As a result, the radiating energy flux depends nonlinearly on the configuration of all topographic steps.

Our model is formulated to obtain solutions over locally flat regions by matching pressure and velocity at topographic discontinuities (Chapman and Hendershott 1981). The matching conditions produce the coupling equations for linear tides model, which we refer to as CELT. CELT is unique because it (i) unambiguously separates the modal solutions to LTE in regions of arbitrary one-dimensional topography, (ii) explicitly solves for leftward- and rightward-propagating tides, and (iii) easily accommodates two-way surface–internal-tide coupling.

a. Resolving incident and reflected tides

Internal tides are generated (e.g., Rattray et al. 1969; Baines 1982), reflected (e.g., Chapman and Hendershott 1981; Nash et al. 2004; Klymak et al. 2011a), scattered (e.g., Müller and Liu 2000; Thorpe 2001; Kelly et al. 2012), and dissipated along the continental margins (e.g., Kunze et al. 2002; Legg and Adcroft 2003; Nash et al. 2007). CELT can be used to determine the amplitudes of transmitted and reflected internal tides, rather than more traditional quantities like velocity and

[1] Note that there is only a pointwise mismatch exactly at the bottom. The projection of any depth profile onto the complete set of vertical modes is uniformly convergent.

pressure. The theoretical framework of the model also enables the separation of directional energy fluxes in both observations and simulations of realistic flows that vary in approximately one horizontal dimension. Directional energy fluxes can determine the exact locations of internal-tide generation, reflection, scattering, and tidally driven mixing over arbitrary topographic shapes. We demonstrate the practical utility of CELT by simulating internal-tide scattering and reflection on the Australian northwest, Brazil, and Oregon continental slopes, which are approximated as along-slope uniform.

b. *Modeling two-way surface–internal-tide coupling*

Historically, most analytical and numerical models have been developed to individually model surface (e.g., Egbert et al. 2004) or internal (e.g., Baines 1982) tides without including two-way surface–internal-tide coupling. These models assume a priori that tide–topography interactions only transfer energy from the surface to the internal tides. The essence of this approximation is summarized by Hendershott (1981):

> I speculate that if oceanic internal modes are sufficiently inefficient as energy transporters that they cannot greatly alter the energetics of the [mode-0] solution unless their amplitudes are resonantly increased beyond observed levels, and if they are sufficiently dissipative that they effectively never are resonant, then an extension of this analysis to realistic basins and relief would probably confirm LTE [for the 0^{th} vertical mode] as adequate governors of the surface elevation. . . . With appropriate allowance for various dissipative processes (including all mechanisms that put energy into internal tides), I regard [LTE for mode-0] as an adequate approximation for studying the ocean surface tide.

However, over the last 30 years, internal tides have been observed to transport energy thousands of kilometers (e.g., Zhao and Alford 2009) and resonate across ocean basins (Dushaw and Worcester 1998) and between ridges (Buijsman et al. 2010). Furthermore, Egbert et al. (2004) estimated global surface-tide energy dissipation using a data-assimilating model and found regions of inexplicable surface-tide energy gain (i.e., work done on the surface tide that could not be explained by the ATGF alone). Although Egbert et al. (2004) dismissed these gains in surface-tide energy as errors, regional numerical simulations have identified regions of surface-tide energy gain that are associated with internal-tide energy loss (e.g., Kurapov et al. 2003; Hall and Carter 2011). In addition, Kelly and Nash (2010) observed energy transfer from an internal tide to the surface tide when an incident internal tide shoaled on the New Jersey continental slope (a process they referred to as internal-tide destruction). Therefore, models of two-way surface–internal-tide coupling are presently necessary to investigate the physics, efficiency, and global significance of internal-to-surface-tide energy conversion.

At present, regional numerical simulations can be used to quantify internal-to-surface-tide energy conversion, but surface-tide dynamics in these models are heavily dictated by boundary conditions (Carter and Merrifield 2007). Conversely, surface tides are well represented in global simulations, but internal tides are not fully resolved and surface–internal-tide coupling is usually subsidized by artificial parameterizations (Arbic et al. 2010). Using CELT, surface and internal tides are represented as waves and surface–internal-tide coupling can be modeled over high-resolution topography. Because CELT treats tide–topography interaction as a scattering problem (i.e., it accepts incident tides and solves for reflected and transmitted tides) and is inherently energy conserving (section 2a), it can accurately estimate the efficiency of internal-to-surface-tide energy conversion over idealized and realistic continental slopes. CELT's most significant limitation is that it only accommodates one horizontal dimension, so it cannot explicitly account for scattering over three-dimensional topography, the generation of coastal-trapped waves, or the reflection of obliquely incident internal tides.

This paper is organized as follows. In section 2, the modal decomposition of LTE is reviewed and CELT is derived. In section 3, the convergence of CELT is examined in terms of vertical modes and topographic steps. In section 4a, CELT is used to make tidal predictions, which are verified by a finite-volume numerical simulation. In section 4b, directional energy fluxes are computed from the finite-volume simulations and CELT solutions. In section 4c, the physics of internal-to-surface-tide energy conversion are investigated along the continental margins. A discussion of the results and applications is presented in section 5.

2. Methods

Over a flat bottom on an f plane (Thomson 1879), LTEs for each vertical mode n are

$$\frac{\partial U_n}{\partial t} - f V_n = -\frac{\partial P_n}{\partial x}, \tag{1a}$$

$$\frac{\partial V_n}{\partial t} + f U_n = 0, \quad \text{and} \tag{1b}$$

$$\frac{\partial P_n}{\partial t} + g H_n \frac{\partial U_n}{\partial x} = 0, \tag{1c}$$

where t is time, x and y are the horizontal coordinates, gradients in the y direction are approximated as zero, g is gravity, f is the inertial frequency, and H_n is the equivalent depth. Horizontal velocities and reduced pressure (i.e., pressure divided by reference density) are defined as

$$(u, v) = \sum_{n=0}^{\infty} (U_n, V_n)\phi_n \quad \text{and} \quad p = \sum_{n=0}^{\infty} P_n \phi_n, \tag{2}$$

respectively. By Fourier transforming (1a)–(1c), U_n, V_n, and P_n may be regarded as complex harmonic amplitudes and time derivatives may be rewritten $\partial/\partial t = -i\omega$, where ω is the tidal frequency. The vertical structure functions ϕ_n and equivalent depths are determined by the eigenvalue problem

$$\frac{\partial}{\partial z}\left(\frac{1}{N^2 - \omega^2}\frac{\partial \phi_n}{\partial z}\right) + \frac{1}{gH_n}\phi_n = 0, \tag{3}$$

where z is the vertical coordinate (positive upward), and N is the buoyancy frequency. The boundary conditions are a free surface and flat bottom. The flat bottom requires the vertical velocity to equal zero at $z = -H$, which dictates $\partial\phi_n/\partial z = 0$ at $z = -H$, via the buoyancy and vertical momentum balances (not shown). The quantity ω^2 is retained in (3) to improve the accuracy of the model by including linear nonhydrostatic effects (a slight departure from LTE). Group speed and horizontal wavenumber for each mode are given as $c_n = \sqrt{(1 - f^2/\omega^2)}\sqrt{gH_n}$ and $k_n = \sqrt{(1 - f^2/\omega^2)}\omega/\sqrt{gH_n}$, respectively.

In the deep ocean, the nondimensional parameter $\in = N^2H/g$, which measures the bottom-to-surface density difference, is normally less than 1%, allowing us to approximate the surface tide with an equivalent depth $H_0 \approx H$ and depth-uniform vertical structure (Pedlosky 2003). This also allows us to approximate the free surface as a rigid lid ($\partial\phi_n/\partial z = 0$ at $z = 0$) when computing the internal-tide modes (i.e., $n \geq 1$). A result of these approximations is that the vertical structure functions are orthogonal over the depth of the water column and do not produce spurious internal-tide generation through the free surface (Kelly et al. 2010).

In practice we solve (3) numerically for modes $n \geq 1$, using the rigid-lid approximation and second-order finite differences. For all modes, the resulting vertical structure functions are orthogonal and scaled so that

$$\frac{1}{H}\int_{-H}^{0} \phi_m \phi_n \, dz = \delta_{mn}, \tag{4}$$

where m and n are modal indices, and δ_{mn} is the Kronecker delta function. The structure functions are also complete [see (2)], so that projections of pressure and velocity onto this basis are uniformly convergent (i.e., variance conserving).

Combining (1a)–(1c) with our definition for k_n produces a one-dimensional Helmholtz equation

$$\frac{\partial^2 U_n}{\partial x^2} + k_n^2 U_n = 0, \tag{5}$$

which has a general solution

$$U_n = a_n e^{ik_n x} + b_n e^{-ik_n x}, \tag{6}$$

where a_n and b_n represent the complex harmonic amplitudes of waves traveling to the right and left, respectively. Substituting (6) into (1c) produces the general solution for pressure

$$P_n = c_n(a_n e^{ik_n x} - b_n e^{-ik_n x}), \tag{7}$$

where ϕ_n, c_n, and k_n can be computed a priori from N^2 and H. It is possible to determine the system [(1a)–(1c)] in terms of either U_n and P_n or a_n and b_n. We will solve for a_n and b_n because they provide information about the direction of wave propagation.

a. Matching solutions at a discontinuity

Horizontal variability in H, N^2, and/or f creates horizontal gradients in the vertical structure functions, group speeds, and horizontal wavenumbers. Here, we model continuous topography as a series of discrete steps, thus creating discontinuities in structure functions, group speeds, and horizontal wavenumbers. A general procedure for matching the wavefield across these discontinuities is to ensure that u and p are continuous (Chapman and Hendershott 1981)

$$u^{(j)} = u^{(j+1)} \quad \text{at} \quad x^{(j)} \quad \text{for} \quad z \in [-H^{(d)}\, 0] \quad \text{and} \tag{8a}$$

$$p^{(j)} = p^{(j+1)} \quad \text{at} \quad x^{(j)} \quad \text{for} \quad z \in [-H^{(s)}\, 0], \tag{8b}$$

where the index j identifies the discontinuity and denotes the solution to the left of the discontinuity.[2] The index $j + 1$ denotes the solution to the right of the

[2] When N is horizontally constant, this procedure is equivalent to matching u and w [i.e., horizontal and vertical velocity, e.g., St. Laurent et al. (2003)]. When N is horizontally variable, matching p generally leads to discontinuous w and vice versa. However, matching p is always dynamically and numerically preferable because it avoids infinite pressure-gradient forces at the steps and converges with fewer modes.

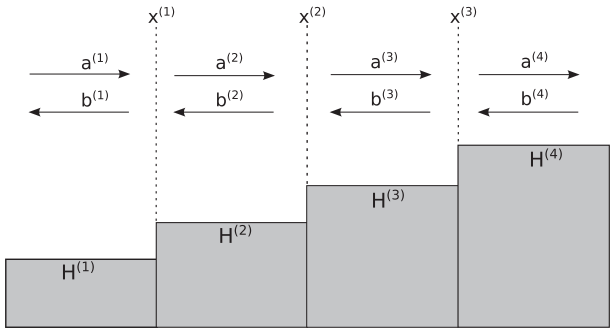

FIG. 1. Schematic of waves propagating over stepwise topography (the variables are defined in the text).

discontinuity (Fig. 1). The superscripts (d) and (s) denote quantities on the deep and shallow sides of the discontinuity, respectively. For example, the values $H^{(d)} = \max[H^{(j)}, H^{(j+1)}]$ and $H^{(s)} = \min[H^{(j)}, H^{(j+1)}]$ are the fluid depths on the deep and shallow sides of the discontinuity. Here, we define velocity as zero below the bottom [i.e., $u^{(j)} = 0$ for $z < H^{(j)}$ for arbitrary j] so that the matching condition for velocity, which extends to the depth of the deeper step, requires $u = 0$ along the vertical wall. The matching condition for pressure, which only extends to the depth of the shallower step, does not constrain pressure along the vertical wall.

Using the orthogonality of the structure functions (4), we project (8a) and (8b) onto each mode m

$$\mathbf{U}^{(jL)}\mathbf{a}^{(j)} + \mathbf{U}^{*(jL)}\mathbf{b}^{(j)} = \mathbf{U}^{(jR)}\mathbf{a}^{(j+1)} + \mathbf{U}^{*(jR)}\mathbf{b}^{(j+1)} \quad \text{and} \tag{9a}$$

$$\mathbf{P}^{(jL)}\mathbf{a}^{(j)} - \mathbf{P}^{*(jL)}\mathbf{b}^{(j)} = \mathbf{P}^{(jR)}\mathbf{a}^{(j+1)} - \mathbf{P}^{*(jR)}\mathbf{b}^{(j+1)}, \tag{9b}$$

where $\mathbf{a}$ and $\mathbf{b}$ are vectors of a_n and b_n, and $\mathbf{U}$ and $\mathbf{P}$ are matrices of coefficients defined as

$$\mathbf{U}_{m,n}^{(jL)} = e^{ik_n^{(j)}x^{(j)}} \int_{-H^{(d)}}^{0} \phi_n^{(j)}\phi_m^{(d)}\,dz\,, \tag{10a}$$

$$\mathbf{U}_{m,n}^{(jR)} = e^{ik_n^{(j+1)}x^{(j)}} \int_{-H^{(d)}}^{0} \phi_n^{(j+1)}\phi_m^{(d)}\,dz\,, \tag{10b}$$

$$\mathbf{P}_{m,n}^{(jL)} = c_n^{(j)} e^{ik_n^{(j)}x^{(j)}} \int_{-H^{(s)}}^{0} \phi_n^{(j)}\phi_m^{(s)}\,dz, \quad \text{and} \tag{10c}$$

$$\mathbf{P}_{m,n}^{(jR)} = c_n^{(j+1)} e^{ik_n^{(j+1)}x^{(j)}} \int_{-H^{(s)}}^{0} \phi_n^{(j+1)}\phi_m^{(s)}\,dz\,. \tag{10d}$$

Here, the matrices $\mathbf{U}$ and $\mathbf{P}$ are all denoted by the index j because they are associated with the discontinuity j. The jL and jR superscripts denote whether $\mathbf{U}$ and $\mathbf{P}$ are associated with the solutions to the left [$\mathbf{a}^{(j)}$ and $\mathbf{b}^{(j)}$] or right [$\mathbf{a}^{(j+1)}$ and $\mathbf{b}^{(j+1)}$] of the discontinuity. Each entry in these matrices is the projection of the nth mode of the rightward-propagating component of u or p onto the mth structure function, which is either taken from the shallow or deep side of the discontinuity. The projection of the leftward-propagating components of u or p is given by the complex conjugates of these matrices. When the nth and mth structure functions are calculated on the same side of the step, the integrals of their products are zero except when $n = m$. When the nth and mth structure functions are calculated on different sides of the step, every integral of their product is nonzero because structure functions at different depths do not have special orthogonality relationships.

By truncating m and n at M, (9) reduces to $2M$ linearly independent equations. For a single step, prescribing the incident-wave amplitudes [$\mathbf{a}^{(j)}$ and $\mathbf{b}^{(j+1)}$] leaves $2M$ unknowns [$\mathbf{b}^{(j)}$ and $\mathbf{a}^{(j+1)}$], which represent the radiated-wave amplitudes (Fig. 1). Therefore, the system can be written as

$$\begin{bmatrix} \mathbf{U}^{*(jL)} & -\mathbf{U}^{(jR)} \\ -\mathbf{P}^{*(jL)} & -\mathbf{P}^{(jR)} \end{bmatrix} \begin{bmatrix} \mathbf{b}^{(j)} \\ \mathbf{a}^{(j+1)} \end{bmatrix} = \begin{bmatrix} -\mathbf{U}^{(jL)}\mathbf{a}^{(j)} + \mathbf{U}^{*(jR)}\mathbf{b}^{(j+1)} \\ -\mathbf{P}^{(jL)}\mathbf{a}^{(j)} - \mathbf{P}^{*(jR)}\mathbf{b}^{(j+1)} \end{bmatrix}, \tag{11}$$

and the radiated-wave amplitudes can be obtained via a matrix inversion. This formulation is more general than previous solutions at a topographic step (e.g., Chapman and Hendershott 1981; St. Laurent et al. 2003; Klymak et al. 2011a) because it (i) incorporates arbitrary stratification and structure functions, (ii) generalizes the forcing function to include waves of any mode from either direction, and (iii) explicitly represents the surface tide as a freely propagating wave [i.e., surface-tide velocity varies spatially and is not prescribed a priori, e.g., St. Laurent et al. (2003)].

The system (11) is energy conserving provided the structure functions on each side of the step are discretized on the same (over resolved) vertical grid. When this is true, velocity and pressure are matched at the discontinuity to the precision of the eigenvalue solver. As a result, total energy flux, which is the product of velocity and pressure summed over all modes, is nondivergent across the discontinuity.

b. Matching solutions at multiple discontinuities

The matching conditions extend to multiple discontinuities in H, N^2, and f by treating radiated waves at the interior steps as incident waves at the adjacent steps. For three discontinuities ($j = 1, 2, 3$; Fig. 1), the coupling equation is only forced by incoming waves at the boundaries

$$\begin{bmatrix} \mathbf{U}^{*(1L)} & -\mathbf{U}^{(1R)} & -\mathbf{U}^{*(1R)} & 0 & 0 & 0 \\ -\mathbf{P}^{*(1L)} & -\mathbf{P}^{(1R)} & \mathbf{P}^{*(1R)} & 0 & 0 & 0 \\ 0 & \mathbf{U}^{(2L)} & \mathbf{U}^{*(2L)} & -\mathbf{U}^{(2R)} & -\mathbf{U}^{*(2R)} & 0 \\ 0 & \mathbf{P}^{(2L)} & -\mathbf{P}^{*(2L)} & -\mathbf{P}^{(2R)} & \mathbf{P}^{*(2R)} & 0 \\ 0 & 0 & 0 & \mathbf{U}^{(3L)} & \mathbf{U}^{*(3L)} & -\mathbf{U}^{(3R)} \\ 0 & 0 & 0 & \mathbf{P}^{(3L)} & -\mathbf{P}^{*(3L)} & -\mathbf{P}^{(3R)} \end{bmatrix} \begin{bmatrix} \mathbf{b}^{(1)} \\ \mathbf{a}^{(2)} \\ \mathbf{b}^{(2)} \\ \mathbf{a}^{(3)} \\ \mathbf{b}^{(3)} \\ \mathbf{a}^{(4)} \end{bmatrix} = \begin{bmatrix} -\mathbf{U}^{(1L)}\mathbf{a}^{(1)} \\ -\mathbf{P}^{(1L)}\mathbf{a}^{(1)} \\ 0 \\ 0 \\ \mathbf{U}^{*(3R)}\mathbf{b}^{(4)} \\ -\mathbf{P}^{*(3R)}\mathbf{b}^{(4)} \end{bmatrix}, \qquad (12)$$

which illustrates the general form of the equation. For an arbitrary number of discontinuities, we write the system as

$$\mathbf{Cs} = \mathbf{f}. \qquad (13)$$

The matrix of coupling coefficients is $\mathbf{C}$. It contains $2M$ rows for each discontinuity, which arise from the equations matching a_n and b_n. For a system with L discontinuities, $\mathbf{C}$ has rank $2LM$. The forcing vector is $\mathbf{f}$, which is predetermined by incident tides at the boundaries, and $\mathbf{s}$ is the vector of complex wave amplitudes (i.e., magnitudes and phases) that satisfy the system. It contains the amplitudes of all leftward- and rightward-propagating waves between the steps, and the radiating waves at the boundaries. The system (13) represents CELT, a generalized expression that describes coupling between the vertical modes that evolve according to LTE in one horizontal dimension.

c. *Vertical viscosity*

Although CELT can be solved without viscosity, linear inviscid internal-tide solutions contain velocity and pressure singularities at critical slopes or where topographic geometry facilitates internal-wave attractors (e.g., Maas et al. 1997). Singularities are not observed in oceanic internal tides because they are attenuated by nonlinear and viscous processes. Here, singularities are removed from solutions by including vertical eddy viscosity, which acts on velocity shear and preferentially attenuates high vertical modes. Eddy viscosity is chosen to be depth dependent and inversely proportional to buoyancy frequency squared

$$A_z = \nu \frac{\overline{N^2} - \omega^2}{N^2 - \omega^2}, \qquad (14)$$

where $\overline{N^2}$ is the depth-averaged buoyancy frequency squared, and ν is equivalent to eddy viscosity when stratification is depth constant. Although this parameterization oversimplifies the vertical distribution of turbulence in the ocean, it has a convenient form that is separable by mode in arbitrary stratification (McCreary 1981), that is,

$$D_n = \frac{1}{H}\int_{-H}^{0} \phi_n \frac{\partial}{\partial z}\left(A_z \frac{\partial u}{\partial z}\right) dz = -\nu \frac{\overline{N^2} - \omega^2}{gH_n} U_n. \qquad (15)$$

Between steps, the horizontal momentum equation describes a balance between deceleration and viscous damping

$$\frac{\partial U_n}{\partial t} = -\nu \frac{\overline{N^2} - \omega^2}{gH_n} U_n, \qquad (16)$$

which is satisfied provided U_n decays exponentially in time. Given the local group speed c_n and step width Δx, the tidal amplitudes (a_n or b_n) that are incident at each step are reduced by the fraction:

$$d_n = e^{-\nu[(\overline{N^2} - \omega^2)/gH_n](\Delta x / c_n)}, \qquad (17)$$

which is incorporated in $\mathbf{C}$ for each mode n at each step. In the tidal solutions presented here, $\nu = 10^{-3}\,\mathrm{m^2\,s^{-1}}$ unless otherwise noted. This viscosity attenuates the high modes, associated with sharply defined beams, but not the low modes, which transport most tidal energy.

d. *Neglected dynamics*

In formulating CELT, we have made several approximations that have simplified or omitted known internal-tide dynamics. Most blatantly, we have removed three-dimensional tidal dynamics, which are relevant for curved and rough topography (e.g., Thorpe 2001; Kunze et al. 2002; Legg 2004), as well as topography that receives obliquely incident internal tides (e.g., Martini et al. 2011; Kelly et al. 2012). However, two-dimensional models are locally applicable along many continental margins and mid-ocean ridges because internal tides refract and often propagate roughly normal to large-scale isobaths. In practice, omitting three-dimensional dynamics simplifies the mathematics of CELT and allows for the unique separation of leftward- and rightward-propagating wavefields.

CELT also neglects nonlinear dynamics. At large spatial scales, weak nonlinear interactions between internal tides and mesoscale currents contribute to internal-tide incoherence (Rainville and Pinkel 2006). At smaller scales, nonlinearity becomes important where internal tides propagate at speeds similar to their induced currents, steepen, and break (when they obtain supercritical Froude numbers; Legg and Adcroft 2003; Klymak et al. 2008, 2011b, 2013). At the smallest scales, tide–topography interactions can directly produce intensely turbulent bottom-boundary layers that dominate kinetic-energy dissipation (e.g., Gayen and Sarkar 2010). Here, we have omitted these dynamics to ensure that CELT is computationally inexpensive and its solutions have a straightforward interpretation as a superposition of linear waves. Therefore, CELT solutions in regions of strong mesoscale dynamics, large tidal excursions, and near-critical topography should be interpreted with prudence.

3. Results

CELT relies on a finite number of vertical modes M and topographic steps L to approximate tidal solutions for continuous vertical stratification over continuous topography. Here, CELT solutions are presented for idealized flows with variable values of M and L. These solutions are then examined to verify known aspects of tidal dynamics. All of the solutions presented here consist of an incident mode-1 internal tide that impacts a continental slope. For convenience, the flows are nondimensionalized with depth $H = 1$, $f = 0$, and an incident mode-1 amplitude $a_1 = 1$. The forcing frequency and constant stratification are chosen so that internal-tide beams have slope $\alpha = 1$ [where $\alpha = \sqrt{(\omega^2 - f^2)/(N^2 - \omega^2)}$] making the topographic slope critical when $s = 1$ (where $s = -\partial H/\partial x$). Viscosity is chosen so that it would equal $\nu = 10^{-3}\,\mathrm{m^2\,s^{-1}}$ for semidiurnal waves in an ocean that is 2000 m deep. The reflection (transmission) coefficients, r (t), are defined as the total reflected (transmitted) energy flux in all modes divided by the incident mode-1 energy flux. The reflection and transmission coefficients that are associated with an individual mode have a mode-number subscript.

a. Modal resolution

The number of vertical modes M used in CELT determines the vertical resolution of the flow field. For a single-step continental slope, incident mode-1 internal tides are reflected in a band of enhanced horizontal velocity that is bordered by upward- and downward-propagating internal-tide beams (Figs. 2a–d). As the height of the slope $\Delta H/H$ decreases, less of the incident internal tide is reflected (Fig. 2e), the band of reflected velocities becomes narrower (Figs. 2a–d), and more vertical modes are needed for the CELT solution to converge (Fig. 2e,f). For slopes with $\Delta H/H < ½$, CELT requires approximately $M \geq H/\Delta H$ modes to resolve mode-1 reflection from topographic steps (Fig. 2f). For slopes with $\Delta H/H > ½$, CELT requires approximately $M \geq H/(1 - \Delta H)$ modes to resolve mode-1 reflection from topographic steps (Fig. 2f). These conditions indicate that CELT must include modes with vertical wavelengths that are smaller than both twice the height of the slope and twice the depth of the shelf. However, when $\Delta H/H < 1/16$ only 2% of the incident energy flux is reflected from the step (Fig. 2e). This result suggests that little energy is transported by the high modes ($n \geq 16$) that are needed to resolve the step.

b. Topographic resolution

The number of topographic steps (i.e., L) used in CELT determines whether the solutions over stepwise topography will resemble those over sloping topography. For instance, CELT horizontal velocity and energy flux converge to those of an analytical model of an internal wave propagating up a slope (Wunsch 1969) as L increases (Fig. 3).[3] In effect, the solution of Wunsch (1969) over a continuously sloping bottom is recoverable from a step-wise topographic profile that does not contain any sloping topography per se.

Mode-1 internal-tide reflection coefficients obtained from CELT are also consistent with those obtained by Müller and Liu (2000) using a ray-tracing model. For supercritical slopes, reflection coefficients increase with slope height (Fig. 4). For very tall slopes, results from CELT and Müller and Liu (2000) diverge by about 5% because CELT solutions transmit energy in the surface mode (i.e., mode 0). Omitting the surface mode from the CELT computations removes this disagreement.

Although CELT results agree with those of Müller and Liu (2000) for low-mode reflection, Müller and Liu (2000) also provide extensive analysis of high-mode reflection. CELT solutions for high-mode incident tides are impractical because they only converge with extremely large numbers of topographic steps L, and the numerical cost of solving (13) is proportional to L cubed. In this respect, the scattering model presented by Müller and Liu (2000), which utilizes ray tracing over smooth topography, may be better suited to examine high-mode scattering. However, the model presented by Müller and Liu (2000) may be less accurate in regions of complicated topography, because unlike CELT, it does not account for internal-tide attractors, which result in closed ray paths.

[3] The incident mode-1 ''slope mode'' derived by Wunsch (1969) is not a pure mode-1 flat-bottom mode, although its projection onto flat-bottom modes is dominated by mode 1.

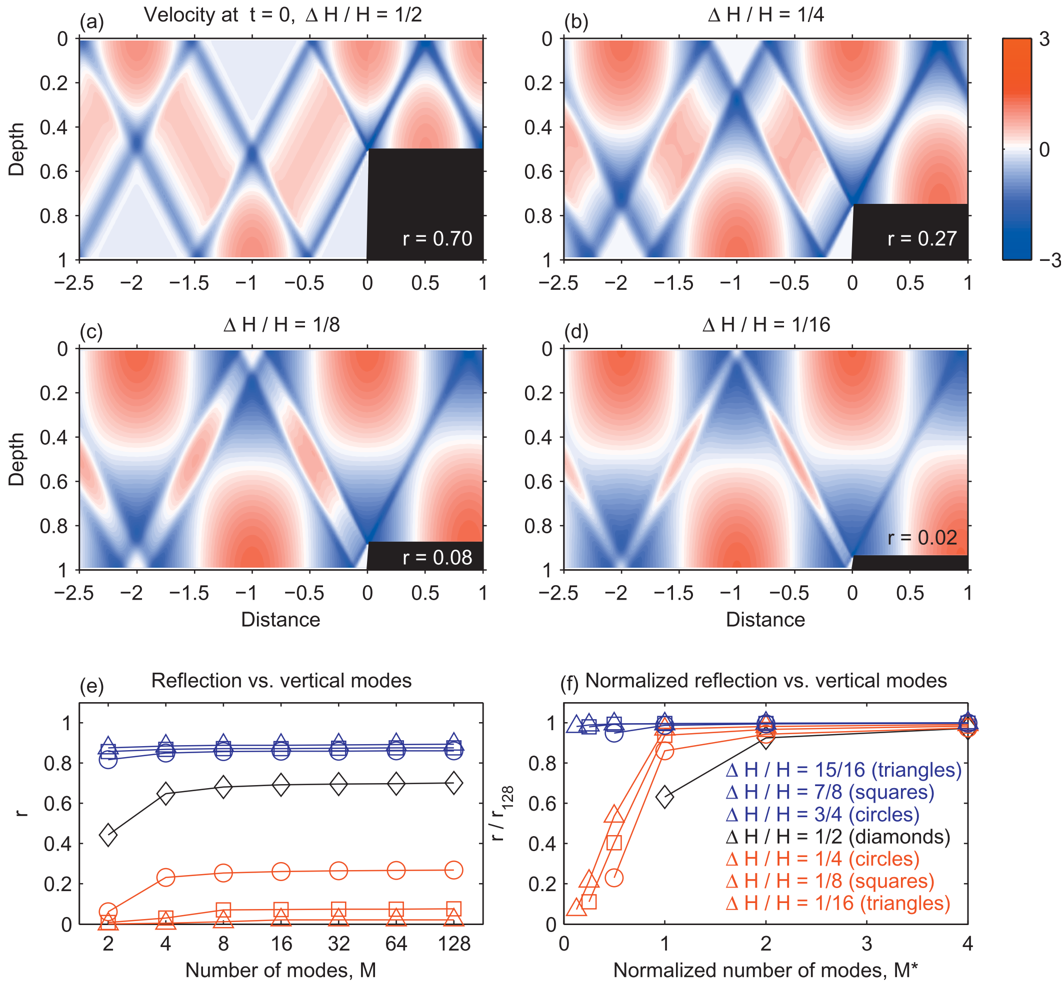

FIG. 2. (a)–(d) CELT model horizontal velocities for an incident mode-1 internal tide at a continental slope approximated by a single topographic step ($M = 128$). Velocities are scaled so that the incident mode-1 amplitude is one (i.e., $a_1 = 1$). Reflection coefficients (i.e., r) decrease with step height and are negligible when $\Delta H/H < 1/16$. (e) For each topographic step, reflection coefficients increase as more modes (i.e., M) are included in the solution. (f) The reflection coefficients approximately converge when $M^* \geq 1$, where $M^* = M/H \times \min(\Delta H, 1 - \Delta H)$.

In general, the interaction of an incident mode-1 tide on a linear slope can be resolved with relatively few steps (e.g., $L \leq 16$; Fig. 5). As a topographic slope is represented by an increasing number of steps, the reflection coefficients for subcritical ($s/\alpha < 1$) slopes decrease to zero ($r = 0$), while the reflection coefficients for supercritical ($s/\alpha > 1$) slopes remain nearly constant ($r \approx r_{\mathrm{step}}$). The reflection coefficients at critical slopes decrease with the number of topographic steps, but do not converge to zero. Reflection coefficients for modes 1 and 2 converge after only a few steps and display trends that are similar to total reflection coefficients (Figs. 5d–i).

These results indicate that the total reflection coefficient at a supercritical slope may be approximated by that of a single topographic step (see, e.g., Garrett and Kunze 2007; Klymak et al. 2011a). Analogously, the reflection coefficient at a subcritical slope (resolved with sufficiently large L) may be approximated as zero, as suggested by ray theory. These results also indicate that inadequately resolved subcritical slopes can produce spurious internal-tide reflection. A pragmatic approach for selecting sufficiently large L, is to ensure that the topographic steps are smaller than the wavelengths of the energy-transporting modes. For an incident mode-1 tide at a single topographic step, $O(95\%)$ of the energy is transported in modes 0–16. To retain this accuracy, L should be increased until individual steps are smaller than the wavelength of the mode-16 vertical-structure function.

Last, CELT can be solved with or without viscosity. Removing viscosity with $L = 64$ has a minimal effect on low-mode transmission and reflection. However,

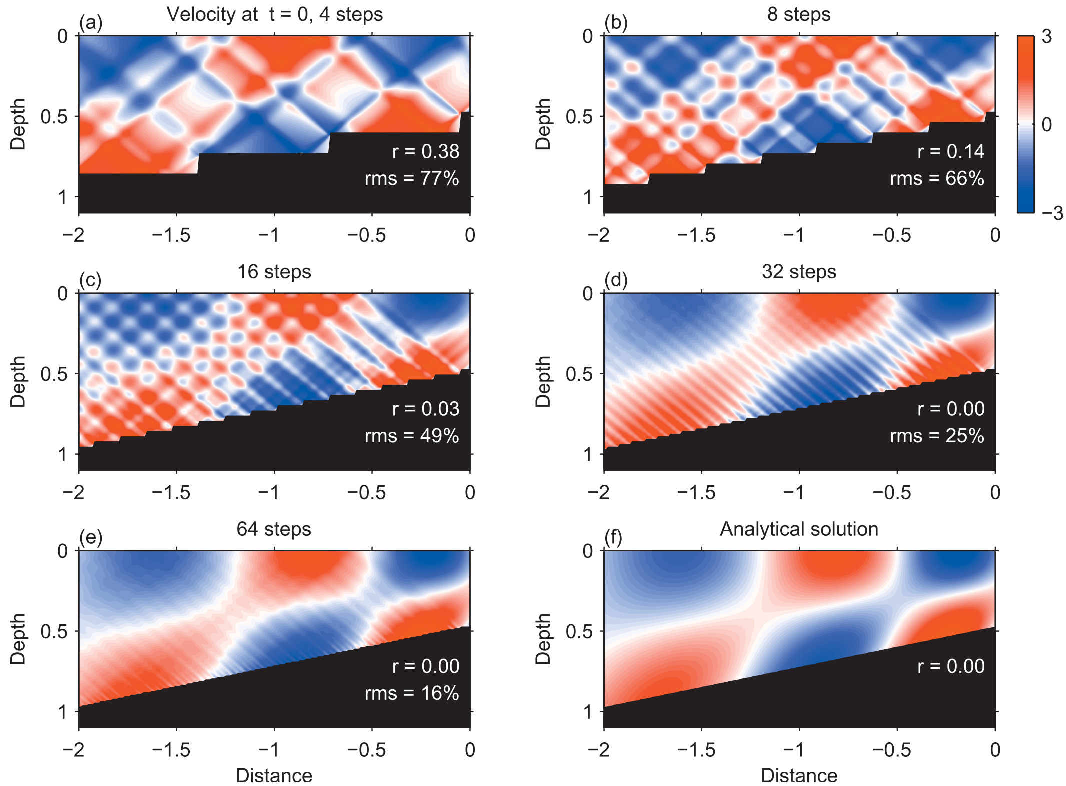

FIG. 3. (a–e) CELT model horizontal velocities ($s = 1/4$, $M = 128$, $a_1 \approx 1$) for a mode-1 "slope mode" converge to (f) the analytical solution (Wunsch 1969) as the number of steps L increases. This convergence is quantified by the decreasing rms difference between the CELT model and analytical solution velocities. Also, as the number of steps increases, reflected energy flux decreases. When $L \geq 64$, negligible energy flux reflects from the slope.

horizontal velocities computed without viscosity contain high-mode noise that is not present in the viscous solutions (i.e., $\nu = 10^{-3}\,\mathrm{m^2\,s^{-1}}$; Fig. 6).

4. Applications

a. *Tidal solutions in realistic settings*

CELT can be configured with realistic forcing, topography, and depth-varying stratification. Here, we predict the reflection of a $250\,\mathrm{W\,m^{-1}}$ mode-1 internal tide that is incident on the Australian northwest (at 19°S in the Browse Basin; Rayson et al. 2011, 2012), Oregon (at 43°N; Moum et al. 2002; Nash et al. 2007; Martini et al. 2011; Kelly et al. 2012; Martini et al. 2013), and Brazil (10°S) continental slopes, which are subcritical, near critical, and supercritical, respectively. CELT is configured with realistic N^2 and f, $\Delta x = 1$ km, $M = 16$, and $\nu = 10^{-3}\,\mathrm{m^2\,s^{-1}}$. For comparison, the Massachusetts Institute of Technology general circulation model (MITgcm; Marshall et al. 1997) is also used to simulate the flows. The MITgcm is configured with 500-m horizontal and 10-m vertical resolution, and $\nu = 10^{-3}\,\mathrm{m^2\,s^{-1}}$. Although the model is written in z coordinates, it employs shaved cells to include piecewise-linear topographic slopes. It enforces free-slip and no-normal flow bottom-boundary conditions. The simulations are analyzed after 30 tidal cycles, when they have reached a semisteady state. A flow relaxation condition is used at the lateral boundaries to prevent the reflection of internal tides that are radiating out of the numerical domain. In practice, the MITgcm simulations take $O(1000)$ times longer to compute than comparable CELT solutions.

For all three slopes, horizontal velocities from CELT and the MITgcm are similar (Figs. 7a–f). Both models indicate that the incident mode-1 internal tides are reflected offshore in several beams. However, CELT solutions are slightly smoother because they have less vertical resolution than the MITgcm solutions. The MITgcm solutions also contain a few steeper beams as a result of higher tidal harmonics generated by finite tidal excursions (Bell 1975; Legg and Huijts 2006) that are explicitly neglected in CELT.

A unique feature of CELT is that solutions can be separated into components that are associated with incident (onshore) and reflected (offshore) wave propagation

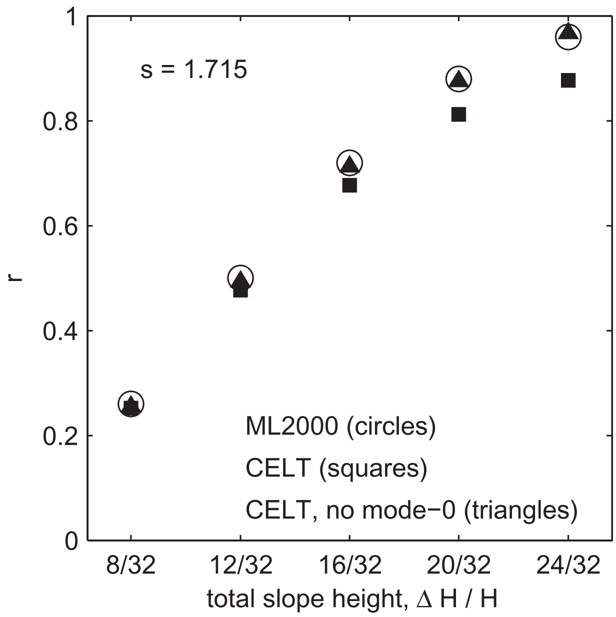

FIG. 4. Reflection coefficients for an incident mode-1 internal tide on a supercritical slope of varying height ($s = 1.725$, $M = 128$, $L = 64$, $\nu = 0$). CELT (squares) underestimates the model of Müller and Liu (2000) (circles; cf. their Fig. 7) except when the surface mode is omitted (triangles).

(Figs. 8a–f). Snapshots of horizontal velocity in the incident wavefields indicate that onshore-propagating mode-1 tides become bottom intensified and form upslope beams where the continental slopes first approach critical steepness (e.g., near the 1800-m isobath on the Australian and Oregon slopes). The reflected wavefields are also intensified over near-critical slopes, indicating that these regions are also the location of partial wave reflection. The Australian slope produces simultaneous incident and reflected propagating beams between the upper and lower shelf breaks, which form a standing wave that was previously identified by Rayson et al. (2012).

Recently, Shimizu (2011) and Kelly et al. (2012) derived a tidally averaged energy balance for individual modes of the internal tide:

$$\frac{\rho_0}{2}\frac{\partial H U_n^* P_n}{\partial x} = \frac{\rho_0}{2}\int_{-H}^{0}\left[u^*\frac{\partial (P_n\phi_n)}{\partial x} - (U_n^*\phi_n)\frac{\partial p}{\partial x}\right] dz, \tag{18}$$

where the left-hand side is the mode-n energy-flux divergence, and the right-hand side is energy conversion into mode n. Only the real component of each term is physically relevant, ρ_0 is the reference density, and the factor of ½ arises by averaging over a tidal period.

On all three continental slopes, the MITgcm simulations indicate that the incident mode-1 tide loses energy by scattering energy to other modes (gray, Figs. 7g–i), which results in mode-1 energy-flux convergence (red, Figs. 7g–i). (Isolated patches of mode-1 energy-flux divergence indicate locations where higher-mode internal tides transfer energy back to the mode-1 tide.) On the Australian northwest and Brazil slopes, most mode-1 scattering occurs onshore of the 1000-m isobath. On the Oregon slope, scattering occurs at three locations where the slope is near critical. In all three MITgcm simulations, mode-1 energy-flux convergence exceeds scattering to other modes because additional tidal energy is lost to nonlinear effects and viscous dissipation. Dissipation and nonlinear processes play the most significant role on the Australian slope because it is wide and known to nonlinearly steepen onshore propagating internal tides (e.g., Van Gastel et al. 2009; Bluteau et al. 2011).

Remarkably, mode-1 energy-flux divergence in CELT (black, Figs. 7g–i) quantitatively balances the magnitudes and spatial distributions of energy conversion to other modes in the MITgcm simulations. The most notable difference between the energy balances of the MITgcm and CELT is that CELT dissipates less energy. CELT dissipates 8%, 5%, and 8% of incident energy flux on the Australian northwest, Oregon, and Brazil slopes, respectively. The MITgcm dissipates 42%, 10%, and 14% of incident energy flux on the respective slopes.

b. *Directional energy fluxes in a numerical simulation*

One benefit of writing velocity and pressure in terms of leftward- and rightward-propagating waves [(6) and (7)] is that these expressions can be rearranged to solve for depth-integrated directional energy fluxes in both numerical simulations and observations that vary in one horizontal dimension. Using CELT, we have shown that flows over sloping topography can be locally approximated as flows over a flat bottom between closely spaced steps. Therefore, full-depth time series of velocity and pressure that are obtained from a mooring or numerical simulation can be decomposed into flat-bottom modes and (6) and (7) can then be inverted to determine the amplitude squared of the left- and right-going wave in each mode. Multiplying these amplitudes by the local group speed produces the right- and left-going energy fluxes:

$$F_n^{(R)} = \frac{\rho_0}{2}c_n H a_n^2 = \frac{\rho_0}{8}c_n H|U_n + P_n/c_n|^2 \quad \text{and} \tag{19}$$

$$F_n^{(L)} = \frac{\rho_0}{2}c_n H b_n^2 = \frac{\rho_0}{8}c_n H|U_n - P_n/c_n|^2, \tag{20}$$

respectively, where $|\cdot|$ represents the complex modulus.

Depth-integrated directional energy fluxes quantify the gross incident and reflected energy fluxes. They

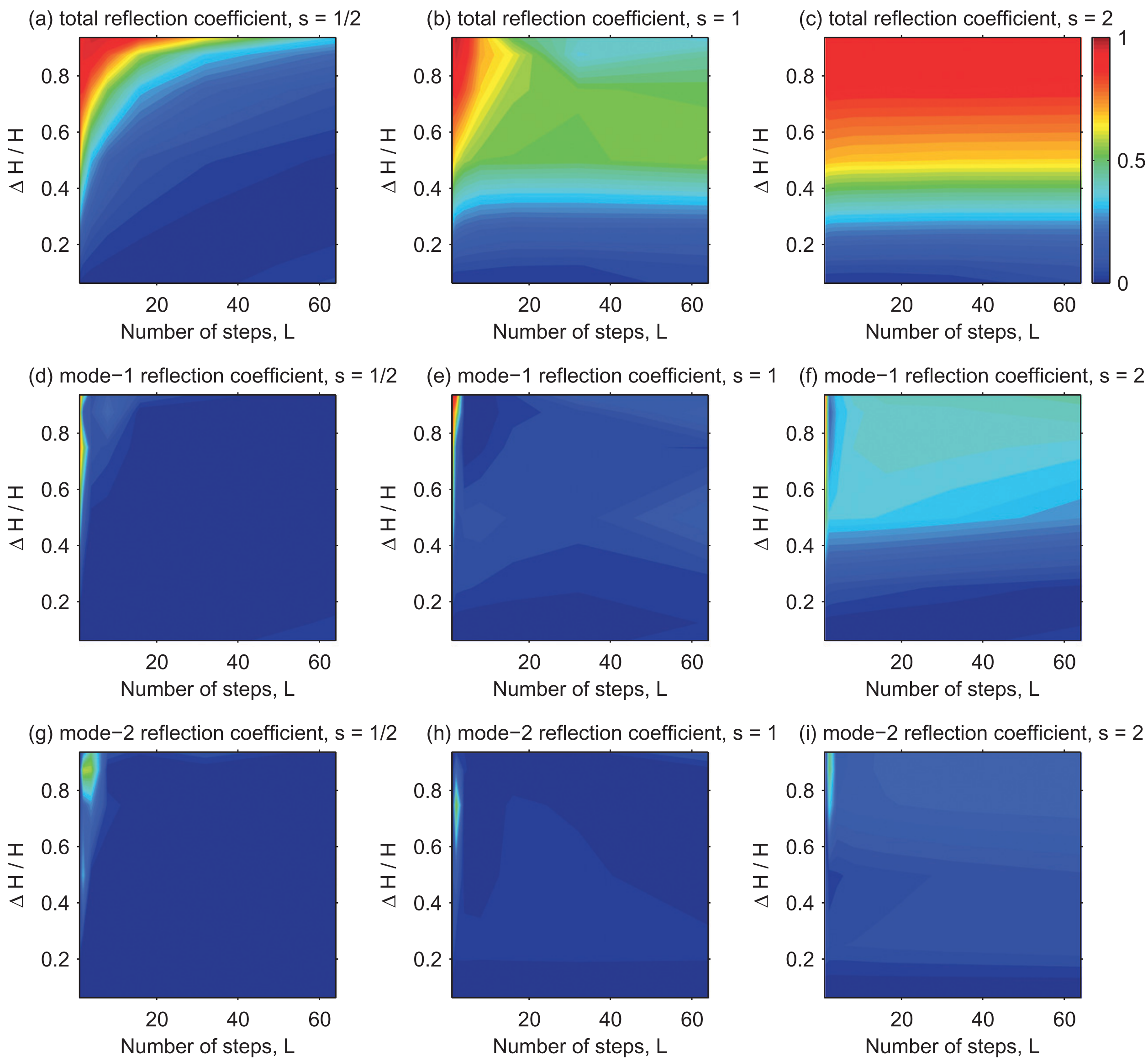

FIG. 5. (a)–(c) Total, (d)–(f) mode-1, and (g)–(i) mode-2 reflection coefficients as a function of topographic steps (i.e., L) and total slope height (i.e., $\Delta H/H$). At subcritical slopes ($s = ½$, $M = 64$, $\nu = 0$) reflection asymptotes to zero as the number of steps increases. At critical slopes ($s = 1$, $M = 64$, $\nu = 0$) reflection asymptotes to a constant as the number of steps increases. At supercritical slopes ($s = 2$, $M = 64$, $\nu = 0$) reflection is approximately constant as the number of steps increases.

can be used to determine the strength and location of internal-tide reflection on a slope. Directional energy fluxes [$F_n^{(R)}$ and $F_n^{(L)}$] that are computed from MITgcm u and p agree with those from CELT (Figs. 8g–i). The most significant disagreement occurs in the offshore energy flux on the Australian slope. Here, the MITgcm simulation has a smaller offshore flux than the CELT solution because dissipation is significantly higher in the MITgcm than CELT (i.e., 42% versus 8% of the incident energy flux). On the Australian northwest and Brazil slopes, most reflection occurs onshore of the 1000-m isobath. On the Oregon slope, reflection occurs gradually over the entire slope. The MITgcm simulations indicate that 44%, 51%, and 84% of incident mode-1 energy flux is reflected in mode 1 by the Australian northwest, Oregon, and Brazil slopes, respectively. Similarly, CELT predicts that 55%, 53%, and 83% of incident energy flux is reflected by these respective slopes. The Oregon slope reflectivity is similar to that obtained in a more realistic three-dimensional simulation of an obliquely incident mode-1 internal tide ($r_1 \approx 60\%$; Kelly et al. 2012).

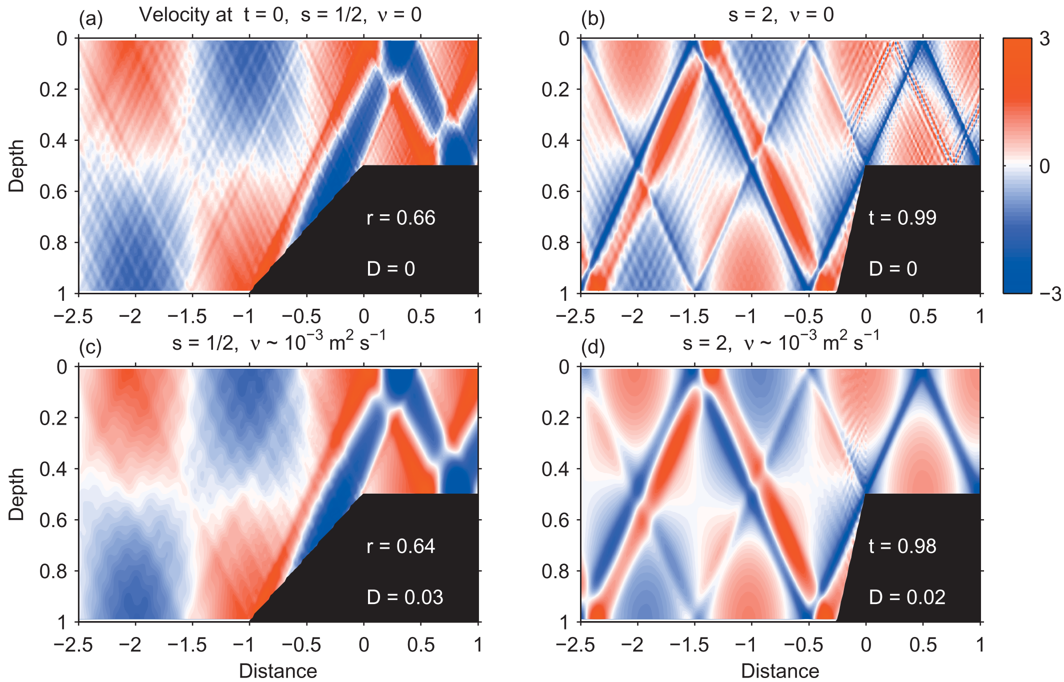

FIG. 6. CELT model horizontal velocities for an incident mode-1 internal tide are weakly affected by viscosity ($M = 128$, $L = 64$, $a_1 = 1$). (a),(b) Solutions without viscosity display a few high-mode beams and no viscous energy dissipation (i.e., $D = 0$). (c),(d) Solutions with viscosity have smoother horizontal velocity and dissipate a small percentage of the incident energy flux.

c. *Surface–internal-tide coupling*

Internal tides generally extract energy from the surface tide, but they can also supply energy (e.g., Kurapov et al. 2003; Hall and Carter 2011; Kelly and Nash 2010). At present, it is unknown what role internal-to-surface-tide energy conversion plays in the global tidal-energy balance. Here, we examine mode-1 internal-tide scattering on continental slopes that are not forced by a surface tide [in contrast to Kelly and Nash (2010)]. In each solution, some energy is transferred from the incident mode-1 tide to a mode-0 tide, producing negative internal-tide generation and spawning a local surface tide.

To estimate the global relevance of internal-to-surface-tide energy conversion, incident mode-1 internal tides were scattered on continental slopes with different heights, depth-uniform stratifications, linear slopes, and continental shelf widths (Fig. 9). These experiments indicate that, when the continental shelf is infinitely wide, the maximum efficiency of from mode-1 to mode-0 scattering is about 5%. Surface-tide generation by incident mode-1 tides is most efficient when the height of the continental slope is about 80% of the total water depth (Fig. 9a), stratification is strong (Fig. 9b), and the topographic gradient is extremely steep (i.e., supercritical; Fig. 9c).

Truncating the width of the continental shelf and including a reflection condition at the coast dramatically alters these results (Fig. 9d). Given optimal slope height, stratification, and steepness, internal-to-surface-tide energy conversion is (i) negligible when the shelf is very thin or close to ½ of a mode-0 wavelength wide and (ii) as large as 15% when the shelf is ¼ of a mode-0 wavelength wide. These results indicate that internal-to-surface-tide energy conversion is sensitive to shelf width, but it is difficult to extend these results to observations because (i) mode-0 wavelengths are variable across realistic continental shelves and (ii) surface tides typically propagate along continental shelves not across them.

Internal-to-surface-tide energy conversion was also estimated on the Australian northwest, Oregon, and Brazil slopes, which have Wentzel–Kramers–Brillouin (WKB)-scaled heights (e.g., Klymak et al. 2011a) of about 70%, 70%, and 90% of the total water depths and top-to-bottom density differences $\Delta\rho$ of 3, 3, and 4 kg m^{-3}, respectively. Estimates of scattering efficiencies from mode 1 to mode 0 for these slopes (with infinitely wide shelves) are 3%, 5%, and 8%, respectively, which roughly agree with the idealized solutions. Therefore, the efficiency of internal-to-surface-tide generation in the absence of surface-tide forcing appears to be on the order of 5%, unless the shelf width facilitates surface-tide resonance.

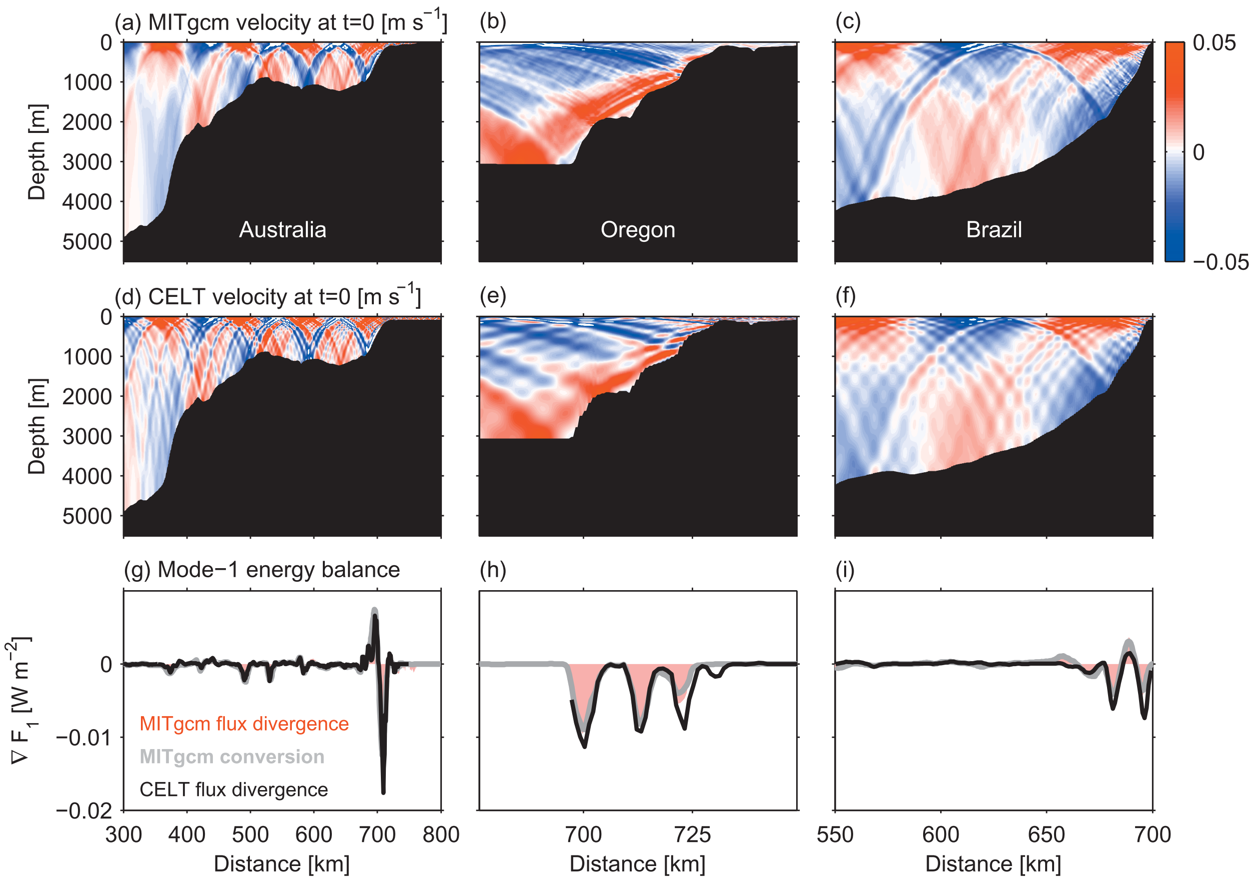

FIG. 7. Horizontal velocity from the MITgcm simulations of a mode-1 internal tide incident on the (a) Australian northwest, (b) Oregon, and (c) Brazil continental slopes compare favorably with (d)–(f) those from the CELT model solutions ($M = 16$, $L = 75$). (g)–(i) In the MITgcm simulations, energy conversion out of mode 1 (gray line) drives mode-1 energy-flux convergence (red shading). The black line indicates the mode-1 energy-flux divergence computed using CELT.

Where continental slopes are forced by surface and incident mode-1 tides, the efficiency of internal-to-surface-tide energy conversion is modulated by the phase difference between the surface and mode-1 tide and can be either negative or much larger than 5% (Kelly and Nash 2010). Therefore, internal-to-surface-tide energy conversion can be highly variable in both space and time. However, we hypothesize that the phase differences between surface and mode-1 tides are uniformly distributed when sampled around the world. As a result, modulation of internal-to-surface-tide energy conversion by local surface-tide forcing is probably negligible in globally integrated energy balances.

5. Discussion

a. The universality of flat-bottom modes

Horizontal velocities and energy fluxes computed between closely spaced steps using CELT agree with those computed over continuously sloping topography (Figs. 3, 7, and 8). As a result, all tidal motions can be interpreted as a superposition of flat-bottom vertical modes that are evolving according to LTE over very small distances. This conceptual view of tidal flow is useful because decomposing tides into the modal solutions of LTE provides a natural method for separating surface and internal tides, examining the vertical structure of energy fluxes (Kunze et al. 2002; Nash et al. 2005), and determining the conversion of tidal energy between quantized vertical wavenumbers (Shimizu 2011; Kelly et al. 2012). Furthermore, only a few vertical modes are needed to efficiently represent the large-scale (e.g., Alford et al. 2007) and energy-transporting portion of the internal tide (e.g., Nash et al. 2006).

Interpreting tides in terms of the modal solutions to LTE is also useful because it permits the separation of leftward- and rightward-depth-integrated energy fluxes in numerical simulations (Fig. 8) and observations of tidal flow in one horizontal dimension. An analogous methodology has been used to separate energy fluxes

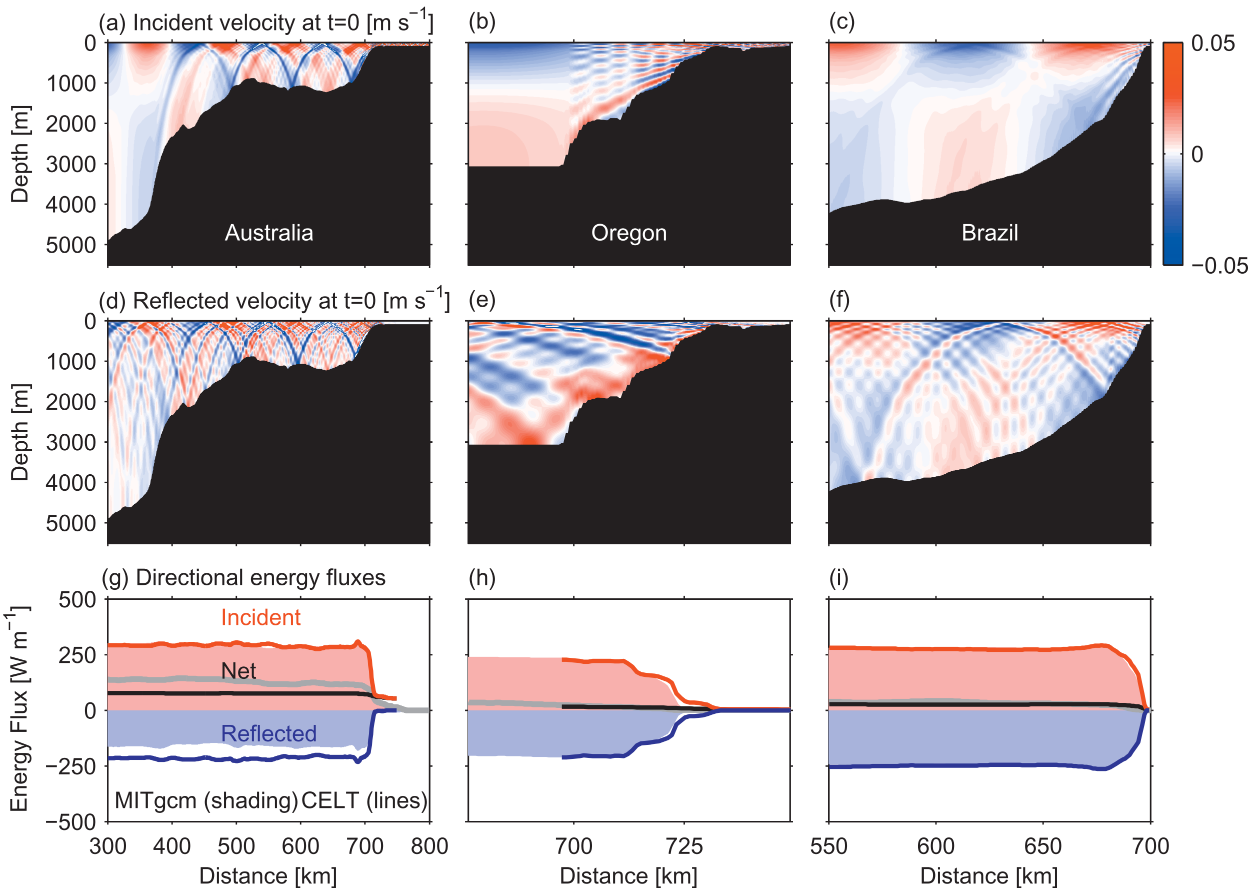

FIG. 8. (a)–(c) Incident and (d)–(f) reflected horizontal velocities from the CELT model solutions indicate the exact locations of reflection and where standing waves develop. (g)–(i) Directional energy fluxes from the MITgcm simulations (shading) are similar to those produced by the CELT model (lines). Net fluxes are the sum of the incident and reflected fluxes.

in observations of shallow-water surface waves (e.g., Sheremet et al. 2002). However, a comprehensive error analysis of contamination by obliquely propagating internal tides is desirable before this method is widely applied to three-dimensional tidal flows.

b. *Tides and bathymetric resolution*

Like previous investigations (e.g., St. Laurent and Garrett 2002; Nash et al. 2006; Griffiths and Grimshaw 2007), results from CELT indicate that most energy is transported by low modes (i.e., $n \leq 16$). Analysis of CELT also indicates that bathymetric steps produce scattering into modes that have vertical wavelengths less than twice the height of the step. Combining these results, and approximating the mode-n vertical wavelength as $\approx 2H/n$, implies that variations in topographic height greater than $H/16$ dictate the linear tidal response. For example, useful bathymetry for a 4000-m-deep ocean should resolve changes in depth greater than 250 m (in a WKB-stretched sense). This resolution is on par with that currently available (Smith and Sandwell 1997). Therefore, it is unlikely that higher-resolution bathymetry will greatly improve predictions of the linear tide at most locations in the deep ocean. However, many global numerical simulations have horizontal grid spacings that are $O(10)$ km (or greater) and do not resolve motions with mode-16 horizontal wavelength. Tidal predictions from these simulations are likely to improve with increased horizontal resolution (Niwa and Hibiya 2011).

A caveat of CELT and other linear models is that they fail to properly describe dissipative processes, which are fundamentally nonlinear and turbulent. The spatial and temporal distribution of tidal-energy dissipation undoubtedly depends on small-scale topography (e.g., Nash et al. 2007; Iwamae and Hibiya 2012) and high-mode tides (e.g., Klymak et al. 2011b). High-resolution topography and fully nonlinear models are necessary to accurately predict tidal dissipation, which drives diapycnal mixing that may affect large-scale ocean circulation (Munk and Wunsch 1998).

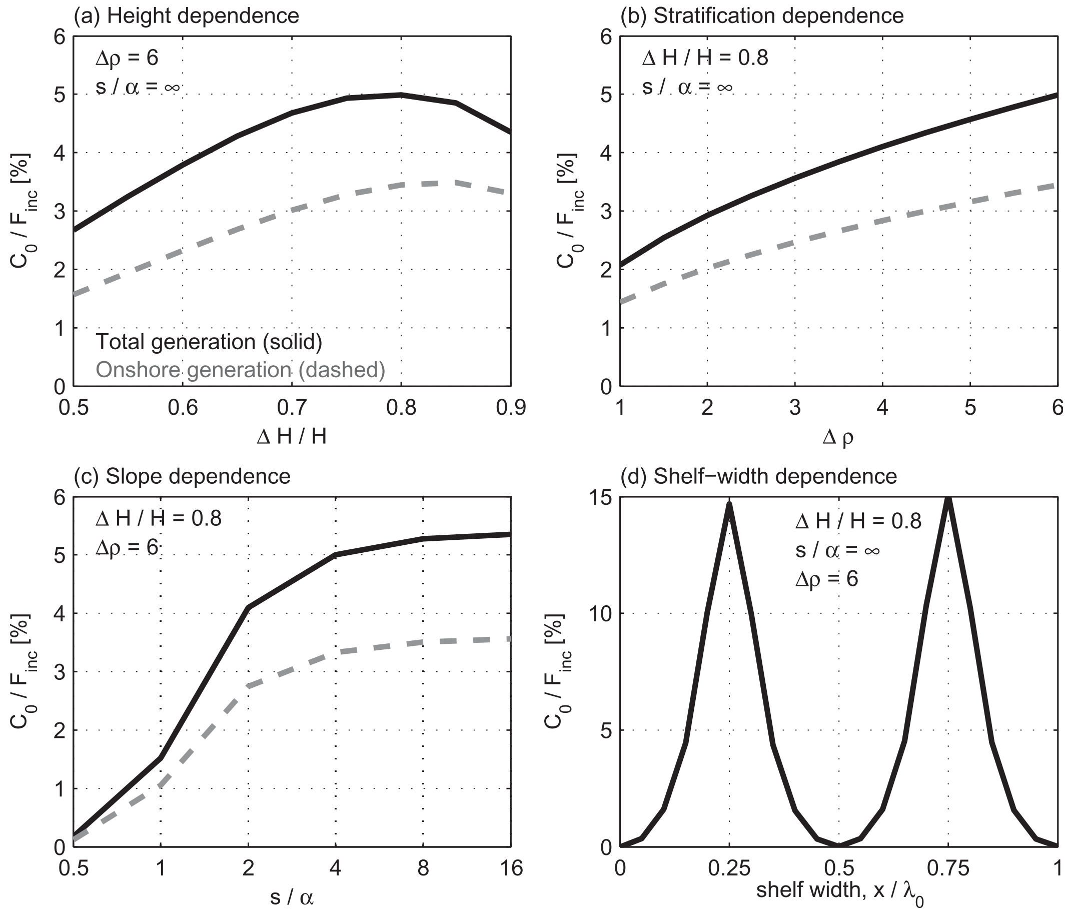

FIG. 9. CELT predictions ($H = 3000\,\mathrm{m}$, $M = 128$, $L = 64$) of internal-to-surface-tide energy conversion by an incident mode-1 internal tide (solid lines) increase with (a) slope height, (b) stratification, and (c) slope steepness when the shelf is infinitely wide. The locally generated surface-tide energy flux is primarily directed toward the coast in (a)–(c) (dotted lines). When the continental shelf is truncated by including tidal reflection at the coast, internal-to-surface-tide energy conversion is sensitive to the width of the shelf (which is normalized by the mode-0 wavelength λ_0).

c. The global tidal-energy balance

Previous estimates of the global tidal-energy balance have examined a one-way energy cascade from surface to internal tides (e.g., Jayne and St. Laurent 2001). Here, we suggest that internal-to-surface-tide energy conversion also occurs, but that its effects are relatively small. Solutions from CELT indicate that, for large continental slopes with strong stratification and infinitely wide shelves, 5% of incident mode-1 energy is transferred to the surface tide. If 85% of internal tides radiate away from their origins (e.g., the Hawaiian Ridge; Rudnick et al. 2003) and eventually strike the continental margins, as much as 2.5% of gross internal-tide generation (i.e., ≈50 GW; Egbert et al. 2004) may be returned to the surface tide. As speculated by Hendershott (1981), this feedback loop is sufficiently weak so that it is unlikely to alter deep-ocean surface-tide predictions. However, surface-tide generation by internal tides could alter surface tides on some continental shelves. For instance, if a $1000\,\mathrm{W\,m^{-1}}$ incident internal tide strikes a continental slope adjacent to a 100-m-deep continental shelf, it could excite a $35\,\mathrm{W\,m^{-1}}$ surface tide that propagates onto the shelf (see Fig. 9). If the surface tide propagates freely, it would have a velocity of $0.03\,\mathrm{m\,s^{-1}}$ and sea surface displacement of 0.1 m, which are measurable. Furthermore, if the phase of the incident internal tide drifts in time because of temporal variability in the mesoscale current field (Rainville and Pinkel 2006), the resulting surface tide would also be incoherent and may contribute to observations of incoherent sea surface displacement (e.g., Colosi and Munk 2006). However, careful investigation of tidal observations is necessary to determine to what extent, if any, incoherent surface tides are the result of incoherent internal tides.

At present, there is no unified theory to explain the decay of the deep-ocean internal tide. As internal tides propagate across ocean basins (Ray and Mitchum 1996), they might decay through wave–wave nonlinear interactions (e.g., St. Laurent and Garrett 2002; MacKinnon and Winters 2005) or scattering at mid-ocean ridges (Johnston et al. 2003) and small-scale roughness (Bühler and Holmes-Cerfon 2011). Alternatively, internal tides may cross the ocean basins with relatively little dissipation (Alford et al. 2007) and then scatter (Müller and Liu 2000; Thorpe 2001; Kelly et al. 2012) and dissipate (e.g., Legg and Adcroft 2003; Martini et al. 2013) along the continental margins. Testing this hypothesis requires knowledge of the incident energy flux and scattering efficiency at each continental slope. CELT is useful in this regard because it can be used to make rapid estimates of tidal scattering in regions of complicated stratification and one-dimensional topography. It could also be used to rapidly examine how varying the phase of an incident internal tide affects internal-tide generation, reflection, transmission, and scattering (Kelly and Nash 2011; Klymak et al. 2011a).

Acknowledgments. S. M. Kelly was supported by a postdoctoral fellowship funded through an AIMS–CSIRO–UWA collaborative agreement. J. D. Nash was supported by NSF Grant OCE0350543. We thank the anonymous reviewers for their insightful comments, which greatly improved the manuscript.

REFERENCES

Alford, M. H., and Z. Zhao, 2007: Global patterns of low-mode internal-wave propagation. Part II: Group velocity. *J. Phys. Oceanogr.,* **37,** 1849–1858.

——, J. A. MacKinnon, Z. Zhao, R. Pinkel, J. Klymak, and T. Peacock, 2007: Internal waves across the Pacific. *Geophys. Res. Lett.,* **34,** L24601, doi:10.1029/2007GL031566.

Arbic, B. K., A. J. Wallcraft, and E. J. Metzger, 2010: Concurrent simulation of the eddying general circulation and tides in a global ocean model. *Ocean Modell.,* **32,** 175–187.

Baines, P. G., 1982: On internal tide generation models. *Deep-Sea Res.,* **29,** 307–338.

Bell, T. H., 1975: Lee waves in stratified flows with simple harmonic time dependence. *J. Fluid Mech.,* **64,** 705–722.

Bluteau, C. E., N. L. Jones, and G. N. Ivey, 2011: Dynamics of a tidally-forced stratified shear flow on the continental slope. *J. Geophys. Res.,* **116,** C11017, doi:10.1029/2011JC007214.

Bühler, O., and M. Holmes-Cerfon, 2011: Decay of an internal tide due to random topography in the ocean. *J. Fluid Mech.,* **678,** 271–293.

Buijsman, M. C., J. C. McWilliams, and C. R. Jackson, 2010: East–west asymmetry in nonlinear internal waves from Luzon Strait. *J. Geophys. Res.,* **115,** C10057, doi:10.1029/2009JC006004.

Carter, G. S., and M. A. Merrifield, 2007: Open boundary conditions for regional tidal simulations. *Ocean Modell.,* **18,** 194–209.

——, and Coauthors, 2008: Energetics of M_2 barotropic-to-baroclinic tidal conversion at the Hawaiian Islands. *J. Phys. Oceanogr.,* **38,** 2205–2223.

Chapman, D. C., and M. C. Hendershott, 1981: Scattering of internal waves obliquely incident upon a step change in bottom relief. *Deep-Sea Res.,* **11,** 1323–1338.

Colosi, J. A., and W. Munk, 2006: Tales of the venerable Honolulu tide gauge. *J. Phys. Oceanogr.,* **36,** 967–996.

Dushaw, B. D., and P. F. Worcester, 1998: Resonant diurnal internal tides in the North Atlantic. *Geophys. Res. Lett.,* **25,** 2189–2192.

Echeverri, P., and T. Peacock, 2010: Internal tide generation by arbitrary two-dimensional topography. *J. Fluid Mech.,* **649,** 247–266.

——, T. Yokossi, N. J. Balmforth, and T. Peacock, 2011: Internal tide attractors between double ridges. *J. Fluid Mech.,* **669,** 354–374.

Egbert, G. D., R. D. Ray, and B. G. Bills, 2004: Numerical modeling of the global semidiurnal tide in the present day and in the last glacial maximum. *J. Geophys. Res.,* **109,** C03003, doi:10.1029/2003JC001973.

Garrett, C., and E. Kunze, 2007: Internal tide generation in the deep ocean. *Annu. Rev. Fluid Mech.,* **39,** 57–87.

Gayen, B., and S. Sarkar, 2010: Turbulence during the generation of internal tide on a critical slope. *Phys. Rev. Lett.,* **104,** 218502, doi:10.1103/PhysRevLett.104.218502.

Gerkema, T., 2011: Comment on ''Internal tide energy over topography'' by S. M. Kelly et al. *J. Geophys. Res.,* **116,** C07029, doi:10.1029/2010JC006611.

Griffiths, S. D., and R. H. J. Grimshaw, 2007: Internal tide generation at the continental shelf modeled using a modal decomposition: Two-dimensional results. *J. Phys. Oceanogr.,* **37,** 428–451.

Hall, R. A., and G. S. Carter, 2011: Internal tides in Monterey Submarine Canyon. *J. Phys. Oceanogr.,* **41,** 186–204.

Hendershott, M. C., 1981: Long waves and ocean tides. *Evolution of Physical Oceanography: Scientific Surveys in Honor of Henry Stommel,* B. A. Warren and C. Wunsch, Eds., The MIT Press, 292–341.

Iwamae, N., and T. Hibiya, 2012: Numerical study of tide-induced mixing over rough bathymetry in the abyssal ocean. *J. Oceanogr.,* **68,** 195–203.

Jayne, S. R., and L. C. St. Laurent, 2001: Parameterizing tidal dissipation over rough topography. *Geophys. Res. Lett.,* **28,** 811–814.

Johnston, T. M. S., M. A. Merrifield, and P. E. Holloway, 2003: Internal tide scattering at the Line Islands Ridge. *J. Geophys. Res.,* **108,** 3365, doi:10.1029/2003JC001844.

Kelly, S. M., and J. D. Nash, 2010: Internal-tide generation and destruction by shoaling internal tides. *Geophys. Res. Lett.,* **37,** L23611, doi:10.1029/2010GL045598.

——, and ——, 2011: Reply to comment by T. Gerkema on ''Internal tide energy over topography.'' *J. Geophys. Res.,* **116,** C09002, doi:10.1029/2011JC007040.

——, ——, and E. Kunze, 2010: Internal-tide energy over topography. *J. Geophys. Res.,* **115,** C06014, doi:10.1029/2009JC005618.

——, ——, K. I. Martini, M. H. Alford, and E. Kunze, 2012: The cascade of tidal energy from low to high modes on a continental slope. *J. Phys. Oceanogr.,* **42,** 1217–1232.

Klymak, J. M., R. Pinkel, and L. Rainville, 2008: Direct breaking of the internal tide near topography: Kaena Ridge, Hawaii. *J. Phys. Oceanogr.,* **38,** 380–399.

——, M. H. Alford, R.-C. Lien, Y. J. Yang, and T.-Y. Tang, 2011a: The breaking and scattering of the internal tide on a continental slope. *J. Phys. Oceanogr.,* **41,** 926–945.

——, S. Legg, and R. Pinkel, 2011b: A simple parameterization of turbulent tidal mixing near supercritical topography. *J. Phys. Oceanogr.,* **40,** 2059–2074.

——, M. Buijsman, S. Legg, and R. Pinkel, 2013: Parameterizing baroclinic internal tide scattering and breaking on supercritical topography: The one- and two-ridge cases. *J. Phys. Oceanogr.,* **43,** 1380–1397.

Kunze, E., L. K. Rosenfeld, G. S. Carter, and M. C. Gregg, 2002: Internal waves in Monterey Submarine Canyon. *J. Phys. Oceanogr.,* **32,** 1890–1913.

Kurapov, A., G. Egbert, J. S. Allen, R. N. Miller, S. Y. Erofeeva, and P. M. Kosro, 2003: The M_2 internal tide off Oregon: Inferences from data assimilation. *J. Phys. Oceanogr.,* **33,** 1733–1757.

Laplace, P.-S., 1776: Recherches sur plusieurs points du systme du monde. *Mem. Acad. Roy. Sci. Paris,* **89,** 177–264.

Legg, S., 2004: Internal tides generated on a corrugated continental slope. Part I: Cross-slope barotropic forcing. *J. Phys. Oceanogr.,* **34,** 156–173.

——, and A. Adcroft, 2003: Internal wave breaking at concave and convex continental slopes. *J. Phys. Oceanogr.,* **33,** 2224–2246.

——, and K. M. H. Huijts, 2006: Preliminary simulations of internal waves and mixing generated by finite amplitude tidal flow over isolated topography. *Deep-Sea Res.,* **53,** 140–156.

Llewellyn Smith, S. G., and W. R. Young, 2002: Conversion of the barotropic tide. *J. Phys. Oceanogr.,* **32,** 1554–1566.

Maas, L. R. M., D. Benielli, J. Sommeria, and F. P. A. Lam, 1997: Observation of an internal wave attractor in a confined, stably stratified fluid. *Nature,* **388,** 557–561.

MacKinnon, J. A., and K. B. Winters, 2005: Subtropical catastrophe: Significant loss of low-mode tidal energy at 28.9°. *Geophys. Res. Lett.,* **32,** L15605, doi:10.1029/2005GL023376.

Marshall, J., A. Adcroft, C. Hill, L. Perelman, and C. Heisey, 1997: A finite-volume, incompressible Navier-Stokes model for studies of the ocean on parallel computers. *J. Geophys. Res.,* **102** (C3), 5753–5766.

Martini, K. I., M. H. Alford, E. Kunze, S. M. Kelly, and J. D. Nash, 2011: Observations of internal tides on the Oregon continental slope. *J. Phys. Oceanogr.,* **41,** 1772–1794.

——, ——, ——, J. D. Nash, and S. M. Kelly, 2013: Internal bores and breaking internal tides on the Oregon continental slope. *J. Phys. Oceanogr.,* **43,** 120–139.

McCreary, J., 1981: A linear stratified ocean model of the equatorial undercurrent. *Philos. Trans. Roy. Soc. London,* **298,** 603–635.

Miles, J. W., 1974: On Laplace's tidal equations. *J. Fluid Mech.,* **66,** 241–260.

Moum, J. N., D. Caldwell, J. D. Nash, and G. Gunderson, 2002: Observations of boundary mixing over the continental slope. *J. Phys. Oceanogr.,* **32,** 2113–2130.

Müller, P., and X. Liu, 2000: Scattering of internal waves at finite topography in two dimensions. Part I: Theory and case studies. *J. Phys. Oceanogr.,* **30,** 532–549.

Munk, W., and C. Wunsch, 1998: Abyssal recipes II: Energetics of tidal and wind mixing. *Deep-Sea Res.,* **45,** 1977–2010.

Nansen, F., Ed., 1902: *Oceanography of the North Pole Basin: Norwegian North Polar Expedition, 1893–1896: Scientific Results.* Vol. 3, Fridtjof Nansen Fund for the Advancement of Science, 427 pp.

Nash, J. D., E. Kunze, J. M. Toole, and R. W. Schmitt, 2004: Internal tide reflection and turbulent mixing on the continental slope. *J. Phys. Oceanogr.,* **34,** 1117–1134.

——, M. H. Alford, and E. Kunze, 2005: Estimating internal wave energy fluxes in the ocean. *J. Atmos. Oceanic Technol.,* **22,** 1551–1570.

——, E. Kunze, C. M. Lee, and T. B. Sanford, 2006: Structure of the baroclinic tide generated at Kaena Ridge, Hawaii. *J. Phys. Oceanogr.,* **36,** 1123–1135.

——, M. H. Alford, E. Kunze, K. I. Martini, and S. M. Kelly, 2007: Hotspots of deep ocean mixing on the Oregon continental slope. *Geophys. Res. Lett.,* **34,** L01605, doi:10.1029/2006GL028170.

Newton, I., 1687: *Philosophiae Naturalis Principia Mathematica.* 1st ed. Royal Society, 1031 pp.

Niwa, Y., and T. Hibiya, 2011: Estimation of baroclinic tide energy available for deep ocean mixing based on three-dimensional global numerical simulations. *J. Oceanogr.,* **67,** 493–502.

Pedlosky, J., 2003: *Waves in the Ocean and Atmosphere*. 1st ed. Springer, 260 pp.

Pettersson, O., 1907: Strumstudien vid osterions portar. *Sven. Hydrogr. Biol. Komm. Skr.,* **3,** 13–37.

Rainville, L., and R. Pinkel, 2006: Propogation of low-mode internal waves through the ocean. *J. Phys. Oceanogr.,* **36,** 1220–1236.

Rattray, M., 1960: On the coastal generation of internal tides. *Tellus,* **12,** 54–62.

——, J. G. Dworski, and P. E. Kovala, 1969: Generation of long internal waves at the continental slope. *Deep-Sea Res.,* **16,** 179–195.

Ray, R. D., and G. T. Mitchum, 1996: Surface manifestation of internal tides generated near Hawaii. *Geophys. Res. Lett.,* **23,** 2101–2104.

Rayleigh, L., 1883: Investigation of the character of the equilibrium of an incompressible heavy fluid of variable density. *Proc. London Math. Soc.,* **s1–15,** 170–177.

Rayson, M. D., M. J. Meuleners, G. N. Ivey, N. L. Jones, and G. Wake, 2011: Internal tide dynamics in a topographically complex region; Browse Basin, Australian North West shelf. *J. Geophys. Res.,* **116,** C01016, doi:10.1029/2009JC005881.

——, N. L. Jones, and G. N. Ivey, 2012: Temporal variability of the standing internal tide in the Browse Basin, Western Australia. *J. Geophys. Res.,* **117,** C06013, doi:10.1029/2011JC007523.

Rudnick, D. L., and Coauthors, 2003: From tides to mixing along the Hawaiian Ridge. *Science,* **301,** 355–357.

Sheremet, A., R. T. Guza, S. Elgar, and T. H. C. Herbers, 2002: Observations of nearshore infragravity waves: Seaward and shoreward propagating components. *J. Geophys. Res.,* **107,** C83095, doi:10.1029/2001JC000970.

Shimizu, K., 2011: A theory of vertical modes in multilayer stratified fluids. *J. Phys. Oceanogr.,* **41,** 1649–1707.

Sjöberg, B., and A. Stigebrandt, 1992: Computations of the geographical distribution of the energy flux to mixing processes via internal tides and the associated vertical circulation in the ocean. *Deep-Sea Res.,* **39,** 269–291.

Smith, W. H. F., and D. T. Sandwell, 1997: Global sea floor topography from satellite altimetry and ship depth soundings. *Science,* **277,** 1956–1962.

St. Laurent, L., and C. Garrett, 2002: The role of internal tides in mixing the deep ocean. *J. Phys. Oceanogr.,* **32,** 2882–2899.

——, S. Stringer, C. Garrett, and D. Perrault-Joncas, 2003: The generation of internal tides at abrupt topography. *Deep-Sea Res. I,* **50,** 987–1003.

Thomson, W., 1879: On gravitational oscillations of rotating water. *Proc. Roy. Soc. Edinburgh,* **10,** 92–100.

Thorpe, S. A., 2001: Internal wave reflection and scatter from sloping rough topography. *J. Phys. Oceanogr.,* **31,** 537–553.

Van Gastel, P., G. N. Ivey, M. J. Meuleners, J. P. Antenucci, and O. Fringer, 2009: The variability of the large-amplitude internal wave field on the Australian North West shelf. *Cont. Shelf Res.,* **29,** 1373–1383.

Wunsch, C., 1969: Progressive internal waves on slopes. *J. Fluid Mech.,* **35,** 131–144.

——, 1975: Internal tides in the ocean. *Rev. Geophys. Space Phys.,* **13,** 167–182.

Zeilon, N., 1912: On tidal boundary-waves and related hydrodynamical problems. *K. Sven. Vetenskapsakad. Handlingar,* **4,** 1–46.

Zhao, Z., and M. H. Alford, 2009: New altimetric estimates of mode-1 M_2 internal tides in the central North Pacific Ocean. *J. Phys. Oceanogr.,* **39,** 1669–1684.